Global Sensitivity Analysis for Integrated Heat and Electricity Energy System

Yibo Li, *Student Member, IEEE*, Yijun Xu, *Senior Member, IEEE*, Shuai Yao, Shuai Lu, Wei Gu, *Senior Member, IEEE*, Lamine Mili, *Life Fellow, IEEE*, and Mert Korkali, *Senior Member, IEEE*

***Abstract*—Although global sensitivity analysis (GSA) is gaining increasing popularity in power systems due to its ability to measure the importance of uncertain inputs, it has not been explored in the integrated energy system (IES) in the existing literature. Indeed, when coupled multi-energy systems (e.g., heating networks) are considered, the power system operation states are inevitably altered. Accordingly, its associated GSA, which relies on Monte Carlo simulations (MCS), becomes even more computationally prohibitive since it not only increases the model complexity but also faces large uncertainties. To address these issues, this paper proposes a double-loop generalized unscented transform (GenUT)-based strategy that, for the first time, explores the GSA in the IES while simultaneously achieving high computing efficiency and accuracy. More specifically, we first propose a GenUT method that can propagate the moment information of correlated input variables following different types of probability distributions in the IES. We further design a double-loop sampling scheme for GenUT to evaluate the GSA for correlated uncertainties in a cost-effective manner. The simulations of multiple heat- and power-coupled IESs reveal the excellent performance of the proposed method.**

***Index Terms*—Double-loop sampling, generalized unscented transformation, global sensitivity analysis, integrated energy system.**

I. Introduction

THE IES combines various types of energy systems, including electricity, heat and gas systems, to meet multiple demands for energy consumption and improve energy efficiency [1], [2]. Obviously, it benefits from the diversity of resources and the flexibility of operation through the coupling components between different systems, such as the combined heat and power (CHP) units in the electrical heating system (HN) [3]. However, the dimension of uncertainty also increases due to the complicated integration between several energy systems, whose fluctuated states must be considered accordingly to ensure secure operation of the IES [4]. Therefore, stochastic analysis (e.g., probabilistic energy flow (PEF)) has recently been advocated in the literature to evaluate the uncertain nature of IESs [5].

Y. Li, Y. Xu, S. Lu, and W. Gu are with the Electrical Engineering Department, Southeast University, Nanjing, Jiangsu 210096, China (e-mail: {liyibo, yijunxu, wgu}@seu.edu.cn).

S. Yao is with the School of Engineering, Cardiff University, UK, CF24 3AA (e-mail: YaoS8@cardiff.ac.uk).

L. Mili is with the Bradley Department of Electrical and Computer Engineering, Virginia Tech, Northern Virginia Center, Falls Church, VA 22043 USA (e-mail: lmili@vt.edu).

M. Korkali is with the University of Missouri, Department of Electrical Engineering and Computer Science, Columbia, MO 65211 USA (e-mail: korkalim@missouri.edu).

This work was supported by the National Natural Science Foundation of China under Granted No. 52325703.

(Corresponding author: Yijun Xu.)

Apparently, the PEF computing procedure will have a foreseeable high computational burden if we take into account all the variabilities [6]. This is unnecessary since some variabilities may have little impact on the system operating states, which can be simply ignored while preserving accurate uncertainty analysis results. This is why sensitivity analysis (SA) is well used by researchers in uncertainty quantification (UQ) to measure the importance of the system inputs with respect to their impact on the system outputs. In general, SA methods can be classified into two categories, namely, local sensitivity analysis (LSA) and GSA [7], [8]. The former estimates the sensitivity through the derivative of the system output in terms of the input variable. Although simple, it loses its accuracy when the system is nonlinear, as it contains only information in proximity to the IES operating point [9]. The latter (i.e., GSA) aims to estimate the importance of every input variable related to the uncertainty of the model output. As this article explains, when nonlinearity in the system cannot be ignored, GSA can better determine the sensitivity of the system output to the full range of input variables.

To realize the GSA, a prerequisite based on the uncertainty propagation technique quantifies the variances generated in the output variables as a result of variations in the input variables [10]. Due to this, traditional MCS inevitably suffers from a prohibitive computing burden. So, it comes as no surprise that some surrogate-based methods have been proposed. More specifically, Xu *et al.* [11] first proposed a polynomial chaos expansion (PCE) surrogate model to alleviate computing costs in GSA analysis in power systems. It successfully ranks the critical priority for renewable energy generation that affects the voltage saddle point. Wang *et al.* [12] further extended this surrogate model associated with the principal component analysis to investigate the impacts of uncertainties on microgrids. Furthermore, using a Gaussian process emulator, also known as the Kriging model [13], [14], Ye *et al.* [15] analyzed the Sobol index of the distribution system voltages with respect to stochastic photovoltaics (PV) and load variations. Although surrogate models can alleviate the computational burden of evaluating a large number of samples, their construction can still require additional time, particularly for dimension-sensitive surrogate models such as PCE, where the curse of dimensionality cannot be neglected. Moreover, despite the ability of surrogate models to emulate the behavior of physical models, they still exhibit discrepancies from the actual models, resulting in inevitable errors to some degree.

Although previous work has primarily relied on surrogate models for assessing the GSA, we discovered that there is an-

other approach. Alternatively, among various UQ techniques, the unscented transformation method is known for its cost-effectiveness [16]. However, its exploration within the GSA framework of power systems remains unachieved, let alone the GSA of the IES, which is the focus of our research. [17], [18]. Despite the fact that the traditional unscented transformation (TUT) method has been criticized for failing to provide complete probability density functions (PDFs) of a system's states in probabilistic power flow analysis, it is indeed quite suitable for GSA, which only requires variance to be estimated from the UT for its associated criteria (e.g., the Sobol and Kucherenko indices) [17]. However, designing a UT-based scheme within the GSA framework remains a challenge. Indeed, on the one hand, the traditional UT method is designed only for Gaussian variables that cannot be guaranteed in practice [19]. On the other hand, the precise sampling strategy for UT-based methods to analyze GSA indices for independent and correlated inputs remains an open problem in power systems.

To address the above challenges, we propose a novel double-loop GenUT-based strategy that explores the GSA in the IES for the first time. The simulation results reveal the excellent performance of the proposed method in the GSA of the IES. The main contributions of this paper are summarized below.

- Considering that the coupling of the HN can have an impact on the power system operation states where their intrinsic uncertainties from the loads and renewables are also non-negligible, we investigate the GSA for the IES for the first time.
- To overcome the difficulties of the TUT method in handling correlated non-Gaussian distributions, we propose utilizing a GenUT method that is able to adapt to the statistics of most probability distributions (e.g., Weibull and Beta). Also, it matches higher moments (i.e., the skewness and kurtosis) of non-Gaussian uncertainties than TUT, which assures high computing accuracy [20].
- To analyze the GSA of the IES in a GenUT manner, we further designed a double-loop sampling scheme that can be perfectly merged with the GenUT framework, allowing us to analyze the Sobol index for the correlated inputs in a computationally efficient way [21].

The remainder of this paper is organized as follows. The IES is introduced in Section II. GSA for IES is presented in Section III. A novel GSA framework based on GenUT is proposed in Section IV. The simulation results are presented in Section V, followed by the conclusions in Section VI.

II. Probabilistic Energy Flow Analysis for IES

In this section, we formulate the IES model considering the coupling facilities and the coupling mode between the power system and the HN. Then, we describe the uncertainties in IES for its probabilistic analysis.

A. Formulations of the HN and Power System

1) The Heating Network (HN)

According to the flow balance and energy conservation constraints, the energy flow equations in the HN are expressed as [22], [23]

$$T_i^{\mathrm{out}} - T^{\mathrm{a}} = \left(T_i^{\mathrm{in}} - T^{\mathrm{a}}\right) \cdot e^{-\frac{\lambda L}{c\dot{m}_i}}, \quad \forall i \in \mathbb{E}, \tag{1}$$

$$\sum_i \left(\dot{m}_{d,i}^{\mathrm{in}} \cdot T_{d,i}^{\mathrm{in}}\right) = T_d \cdot \sum_i \dot{m}_{d,i}^{\mathrm{in}}, \quad \forall d \in \mathbb{V}^{\mathrm{i}},\ i \in \mathbb{E}_d^{\mathrm{in}}, \tag{2}$$

$$T_{d,j}^{\mathrm{out}} = T_d, \quad \forall d \in \mathbb{V}^{\mathrm{i}},\ j \in \mathbb{E}_d^{\mathrm{out}}, \tag{3}$$

$$\varphi_i = c\dot{m}_i(T_i^{\mathrm{s}} - T_i^{\mathrm{r}}), \quad \forall i \in \mathbb{E} \cup \mathbb{V}. \tag{4}$$

Here, T_i^{in} denotes the temperature of the water when it flows into the ith pipe while T_i^{out} denotes the temperature of the water when it flows out of the ith pipe. T^{a} denotes the ambient temperature outside the HN. $\mathbb{E}/\mathbb{V}$ denotes the set of all pipes/nodes in the HN; $\mathbb{E}_d^{\mathrm{in}}/\mathbb{E}_d^{\mathrm{out}}$ denotes the set of pipes with water flowing into/out of Node d; $\mathbb{V}^{\mathrm{i}}$ denotes the set of nodes at both ends of Pipe i; $\dot{m}_i$ is the mass flow rate of water in the ith pipe while $\dot{m}_{d,i}^{\mathrm{in}}$ is the mass flow rate of water in the ith pipe flowing into Node d; $T_{d,i}^{\mathrm{out}}$ denotes the temperature of water at Node d when it flows out of the ith pipe; $T_i^{\mathrm{s}}/T_i^{\mathrm{r}}$ is the temperature of supply/return water in the ith pipe; φ_i is the injected heat power at Node i or extracted heat power flow in Pipe i; the parameter c is the specific heat capacity of water; λ is the overall heat transfer coefficient of each pipe per unit length; and L represents the pipe length.

In addition, (1) shows that when water flows through a pipe, its temperature drops exponentially along with the length of the pipe. Equation (2) calculates the temperature of the mixture after the water from multiple pipes mixes at the same node. Equation (3) means that the temperature of the water that flows out of the same pipe while injecting into different branches remains the same. Equation (4) reveals that the heat power at Node i is determined by the mass flow and the temperature difference between the supply and return water.

Moreover, since the loop-pressure equation should be satisfied for closed-loop pipes [24], we have

$$\boldsymbol{B}\boldsymbol{K}\,\mathrm{diag}\left(\dot{\boldsymbol{m}}\right)|\,\dot{\boldsymbol{m}}| = \boldsymbol{0}, \tag{5}$$

where $\boldsymbol{B}$ is the loop incidence matrix that links the loop to the pipes. The associated elements are set to $+1/-1$ to define the same/opposite direction of the flow. Additionally, when the pipe is not part of the loop, it is set to 0; $\boldsymbol{K}$ is a diagonal matrix with the resistance coefficients of each pipe on its main diagonal, determined mainly by diameter and flow velocity; $\dot{\boldsymbol{m}}$ is the vector of mass flow within each pipe; and $\mathrm{diag}\left(\boldsymbol{x}\right)$ is the operator that returns a diagonal matrix with the elements of vector $\boldsymbol{x}$ on its main diagonal. Equation (5) also states that the sum of head losses in a closed loop must be zero. Fig. 1 gives an example of a simple HN with one loop. Here, water flows from the heat source at high temperature, bringing heat to heat loads through the supply pipes. Then, the water flows out of heat loads with low temperatures. It finally flows back to the heat source, completing a circulation in a HN.

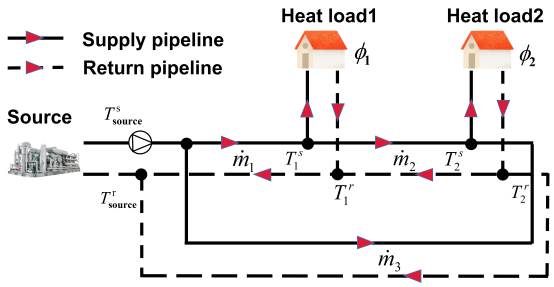

Fig. 1: A simple HN with a loop.

2) The Power System

The AC power flow model of power systems is expressed as [25]

$$P_{G,k} - P_{D,k} = V_k \sum_{i=1}^{m} V_i (G_{ki}\cos(\delta_{ki}) + B_{ki}\sin(\delta_{ki})), \quad (6)$$

$$Q_{G,k} - Q_{D,k} = V_k \sum_{i=1}^{m} V_i (G_{ki}\sin(\delta_{ki}) - B_{ki}\cos(\delta_{ki})), \quad (7)$$

where m is the bus number; $P_{G,k}$ and $Q_{G,k}$ denote the active and reactive power injections at Bus k, respectively; $P_{D,k}$ and $Q_{D,k}$ denote the active and reactive power consumed at Bus k, respectively; V_i and V_k are the voltage magnitudes at Buses i and k, respectively; δ_{ki} represents the angle difference between Buses k and i; G_{ki} and B_{ki} are the conductance and susceptance of the line between Buses k and i, respectively.

B. The Coupling Facilities and Coupling Mode of the IES

The power system and the HN are linked through coupling facilities, including backpressure CHP units, electric boilers, and heat pumps. These coupling facilities work as electrical and heat interfaces with different heat-to-power ratios. Their models can be described as [26]

$$\varphi^{\mathrm{bp}} = P^{\mathrm{bp}}\eta^{\mathrm{bp}}, \quad (8)$$

$$\varphi^{\mathrm{eb}} = P^{\mathrm{eb}}\eta^{\mathrm{eb}}, \quad (9)$$

$$\varphi^{\mathrm{hp}} = P^{\mathrm{hp}}\mathrm{COP}^{\mathrm{hp}}, \quad (10)$$

where superscript bp/eb/hb represents the backpressure unit/-electric boiler/heat pump, respectively. φ and P represent heat/electrical power of coupling facilities, $\eta^{\mathrm{bp}}/\eta^{\mathrm{eb}}/\mathrm{COP}^{\mathrm{hp}}$ represents the heat-to-power ratio of CHP/efficiency of an electric boiler/efficiency of a heat pump, respectively.

More specifically, to assess the impacts of HN on the operating states of the power system, we adopt the operating mode of these two systems as suggested by Yao *et al.* [27]. Here, the coupling mode depends on whether the coupling node serves as the slack bus in the power system or the HN, as the slack bus is utilized to compensate for the unbalanced power between the supply and demand sides.

If one of the coupling nodes serves as the slack node of the HN, its heat power output is first determined by solving the HN energy flow model. Then, its coupled electric power is determined by the ratio of heat and electricity power (8), (9), and (10). If none of the coupling facilities serves as the slack bus of the power systems, the coupling facilities should serve as PV buses if they are CHPs or PQ buses if they are electric boilers or heat pumps. The whole computing process can be summarized as follows: HN $\rightarrow$ coupling facilities $\rightarrow$ power system, as was derived in [27]. This procedure is also summarized in Fig. 2, where the components of an IES are presented in detail.

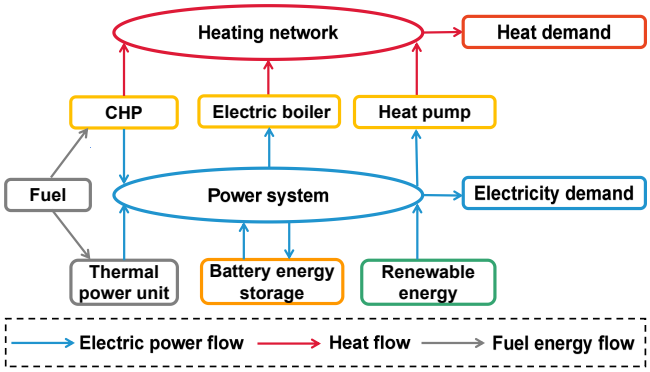

Fig. 2: Plots for the components of the IES system that consist of CHP units, the electric boiler, the heat pump, the traditional thermal power unit, the battery energy storage and the renewable energy generation. Among them, the batteries exchange the electrical energy with the power system through the charging and discharging processes. Electric boilers and heat pumps can transform electricity into heat energy, while CHP units can generate both heat and power. Their associated coupling facilities act as a bridge connecting the power system and the HN in this IES.

C. Uncertainties in IES

1) Loads

In IES, electrical load demands are uncertain. We assume electrical loads have constant power factors and the active power of electrical loads follows a normal distribution as [28]

$$p(\psi^{\mathrm{lp}}) = \frac{1}{\sqrt{2\pi}\sigma_{\psi^{\mathrm{lp}}}} \exp\left[-\frac{\left(\psi^{\mathrm{lp}} - \mu_{\psi^{\mathrm{lp}}}\right)^2}{2{\sigma_{\psi^{\mathrm{lp}}}}^2}\right], \quad (11)$$

where p denotes the PDF; ψ^{lp} represents the active power of electrical loads; $\mu_{\psi^{\mathrm{lp}}}$ and $\sigma_{\psi^{\mathrm{lp}}}$ denote the mean and standard deviation of active power of electrical loads.

In addition, we consider the uncertainties in the HN. We assume the heat loads at every node, namely, one district HN, also follow a normal distribution as [29], [30]

$$p(\varphi^{\mathrm{lp}}) = \frac{1}{\sqrt{2\pi}\sigma_{\varphi^{\mathrm{lp}}}} \exp\left[-\frac{\left(\varphi^{\mathrm{lp}} - \mu_{\varphi^{\mathrm{lp}}}\right)^2}{2{\sigma_{\varphi^{\mathrm{lp}}}}^2}\right], \quad (12)$$

where φ^{lp} represents heat power; $\mu_{\varphi^{\mathrm{lp}}}$ and $\sigma_{\varphi^{\mathrm{lp}}}$ denote the mean and standard deviation of heat power.

2) Wind Generation

The wind generation is widely considered in the probabilistic power flow [31]. The wind speed in the long timescale is commonly described by the Weibull distribution as follows[1]:

[1]The probability distribution is a statistical concept over a long timescale, so it hardly varies in the short term [28]. If the parameters of the input probability distributions vary, we need to reconduct the GSA.

$$p(v)=\begin{cases}\frac{k}{\lambda}(\frac{v}{\lambda})^{k-1}e^{-(v/\lambda)^k} & v\geq 0\\ 0 & v<0\end{cases}, \tag{13}$$

where v represents the wind speed and λ is the scale parameter and k is the location parameter. Furthermore, following [32] its relationship with the active power of a wind farm, P_w, can expressed as

$$P_w=\begin{cases}0 & v\leq v_{\text{ci}}\\ C_1\left(v-v_{\text{ci}}\right) & v_{\text{ci}}<v\leq v_r\\ P_r & v_r\leq v\leq v_{\text{co}}\\ 0 & v>v_{\text{co}}\end{cases}, \tag{14}$$

where v_{ci} is the cut-in wind speed, v_r is the rated wind speed, v_{co} is the cut-out wind speed and P_r is the rated active power output of a wind farm. Here, the slope C_1 is given by

$$C_1=\frac{P_r}{(v_r-v_{\text{ci}})}. \tag{15}$$

3) Solar Generation

Over a long timescale, solar radiation is characterized by the Beta distribution [33] as

$$p\left(r\right)=\frac{\Gamma(\kappa+\varepsilon)}{\Gamma(\kappa)\Gamma(\varepsilon)}\left(\frac{r}{r_{\max}}\right)^{\kappa-1}\left(1-\frac{r}{r_{\max}}\right)^{\varepsilon-1}, \tag{16}$$

where κ and ε are shape parameters, r and $r_{\max}$ are the actual and maximum solar radiations. The active output power of a PV is a function of radiation, which can be expressed as

$$P_s=\begin{cases}\frac{r^2}{r_c r_{\text{std}}}P_d & 0\leq r<r_c\\ \frac{r}{r_{\text{std}}}P_d & r_c\leq r\leq r_{\text{std}}\\ P_d & r>r_{\text{std}}\end{cases} \tag{17}$$

where r_c is the certain radiation point; r_{std} is the rated solar radiation; P_d is the rated power of a PV; and P_s is the active power of a PV.

4) Uncertainty Mitigation

In IES, energy storage helps ensure a continuous and stable power supply from renewable energy generation. Batteries are common storage devices [34], [35]. When wind speed or solar radiation is low, the batteries are discharged as compensation for renewable output power. On the contrary, when the wind speed or solar radiation is high, the batteries are charged to prevent excessive injection of renewable power. The proposed control strategy for battery charging and discharging is defined as [35]

$$P_b=\begin{cases}\tau_{\text{down}}P_n-P_g & P_g<\tau_{\text{down}}P_n\\ \tau_{\text{up}}P_n-P_g & P_g>\tau_{\text{up}}P_n\\ 0 & \tau_{\text{down}}P_n\leq P_g\leq\tau_{\text{up}}P_n\end{cases} \tag{18}$$

where P_b is the output power of the battery; P_g is the actual output power of the renewable generation; P_n is the rated power of the renewable generation; and τ_{down} and τ_{up} are the set coefficients for the lower and upper bounds of the renewable output power, respectively.

Till now, we are able to analyze the PEF by considering the aforementioned uncertainties as [36]

$$\boldsymbol{g}=\boldsymbol{f}\left(x_1,\ldots,x_n\right), \tag{19}$$

where $\boldsymbol{x}=\{x_1,\ldots,x_n\}$ represents n-dimensional random input variables (e.g., loads and renewable generation); $\boldsymbol{g}$ represents random output variables of the system states (e.g., voltage and power).

Remark 1. *Obviously, for an IES consisting of a power system and several district HNs, the operating states of a power system can be impacted by the HNs through the coupling facilities. This also holds in the probabilistic analysis since the HNs have intrinsic uncertainties from the demands. Therefore, the GSA cannot simply ignore coupled HNs while only focusing on a power system for an IES. This is the topic that we will discuss next.*

III. GSA with Correlated Random Inputs

In this section, we first introduce the theory of Sobol indices for variance-based GSA. We then deduce the expressions of the Sobol indices with correlated input variables associated with their computational strategy using MCS.

A. Definition of Variance-based GSA Indices

For (19), let us consider a subset of the variables of $\boldsymbol{x}$, namely $\boldsymbol{y}=(x_1,\ldots,x_s)$, $1\leq s<n$, associated with its complementary subset $\boldsymbol{z}=(x_1,\ldots,x_{n-s})$ so that $\boldsymbol{x}=\{\boldsymbol{y},\boldsymbol{z}\}$. The total variance, D, of $f\left(x_1,\ldots,x_n\right)$ can be decomposed as

$$D=D_y\left[E_{\boldsymbol{z}}\left[f\left(\boldsymbol{y},\bar{\boldsymbol{z}}\right)\right]\right]+E_y\left[D_{\boldsymbol{z}}\left[f\left(\boldsymbol{y},\bar{\boldsymbol{z}}\right)\right]\right], \tag{20}$$

where $E[\cdot]$ and $D[\cdot]$ represent the expectation and the variance of the function. $\boldsymbol{z}$ is generated from a joint PDF, $p(\boldsymbol{y},\boldsymbol{z})$, while $\bar{\boldsymbol{z}}$ is generated from a conditional PDF, $p(\boldsymbol{y},\bar{\boldsymbol{z}}|\boldsymbol{y})$. The ratio

$$S_y=\frac{D_{\boldsymbol{y}}[E_{\boldsymbol{z}}(f(\boldsymbol{y},\bar{\boldsymbol{z}}))]}{D} \tag{21}$$

is known as the first-order Sobol index of $\boldsymbol{y}$ [37], [38]. Its full expression is given by

$$S_y=\frac{1}{D}\left[\int_{\mathbb{R}^s}p(\boldsymbol{y})\,\mathrm{d}\boldsymbol{y}\left[\int_{\mathbb{R}^{n-s}}f(\boldsymbol{y},\bar{\boldsymbol{z}})p(\boldsymbol{y},\bar{\boldsymbol{z}})\,\mathrm{d}\bar{\boldsymbol{z}}\right]^2-f_0^2\right], \tag{22}$$

where f_0 is the total expectation of $f\left(x_1,\ldots,x_n\right)$. Here, a more practical form of calculation is expressed as

$$\begin{aligned}S_y=&\frac{1}{D}\left[\int_{\mathbb{R}^s}p(\boldsymbol{y})\,\mathrm{d}\boldsymbol{y}\left[\int_{\mathbb{R}^{n-s}}f(\boldsymbol{y},\bar{\boldsymbol{z}})p(\boldsymbol{y},\bar{\boldsymbol{z}}\mid\boldsymbol{y})\,\mathrm{d}\bar{\boldsymbol{z}}\right.\right.\\ &\left.\left.\times\int_{\mathbb{R}^{n-s}}f\left(\boldsymbol{y},\bar{\boldsymbol{z}}'\right)p\left(\boldsymbol{y},\bar{\boldsymbol{z}}'\mid\boldsymbol{y}\right)\mathrm{d}\bar{\boldsymbol{z}}'\right]-f_0^2\right].\end{aligned} \tag{23}$$

Implementing (23) requires two groups of samples $\bar{\boldsymbol{z}}$ and $\bar{\boldsymbol{z}}'$ from the conditional distribution of $p(\boldsymbol{y},\bar{\boldsymbol{z}}|\boldsymbol{y})$, respectively.

B. GSA for Gaussian Variables

Now, let us present how to compute S_y under the Gaussian assumption. Assume that $\boldsymbol{\gamma}$ is a vector of n-dimensional normal distributed random variables, namely $\xi_1,\ldots,\xi_n$, its complementary subsets, $\boldsymbol{\alpha}$ and $\boldsymbol{\beta}$, are $\boldsymbol{\alpha}=(\xi_1,\ldots,\xi_s)$, $\boldsymbol{\beta}=(\xi_1\ldots,\xi_{n-s})$. The mean vector and covariance matrix

of γ are $\boldsymbol{\mu}_\gamma$ and $\boldsymbol{\Sigma}_\gamma$, respectively, which can be partitioned as follows:

$$\boldsymbol{\mu}_\gamma = \begin{bmatrix} \boldsymbol{\mu}_{\boldsymbol{\alpha}} \\ \boldsymbol{\mu}_{\boldsymbol{\beta}} \end{bmatrix}, \boldsymbol{\Sigma}_\gamma = \begin{bmatrix} \boldsymbol{\Sigma}_{\boldsymbol{\alpha}} & \boldsymbol{\Sigma}_{\boldsymbol{\alpha\beta}} \\ \boldsymbol{\Sigma}_{\boldsymbol{\beta\alpha}} & \boldsymbol{\Sigma}_{\boldsymbol{\beta}} \end{bmatrix}, \tag{24}$$

where the mean vectors and covariance matrices of $\boldsymbol{\alpha}$ and $\boldsymbol{\beta}$ are $\boldsymbol{\mu}_{\boldsymbol{\alpha}}$, $\boldsymbol{\mu}_{\boldsymbol{\beta}}$ and $\boldsymbol{\Sigma}_{\boldsymbol{\alpha}}$, $\boldsymbol{\Sigma}_{\boldsymbol{\beta}}$. Its conditional distribution, $p\left(\boldsymbol{\alpha}, \bar{\boldsymbol{\beta}} | \boldsymbol{\alpha}\right)$, also follows a normal distribution as

$$p\left(\boldsymbol{\alpha}, \bar{\boldsymbol{\beta}} | \boldsymbol{\alpha}\right) = \phi_{n-s}\left(\boldsymbol{\alpha}, \bar{\boldsymbol{\beta}} | \boldsymbol{\alpha}\right), \tag{25}$$

with its mean vector, $\mu_{\boldsymbol{\beta}c}$, and covariance matrix, $\Sigma_{\boldsymbol{\beta}c}$, as

$$\boldsymbol{\mu}_{\boldsymbol{\beta}c} = \boldsymbol{\mu}_{\boldsymbol{\beta}} + \boldsymbol{\Sigma}_{\boldsymbol{\beta\alpha}} \boldsymbol{\Sigma}_{\boldsymbol{\alpha}}^{-1} (\boldsymbol{\alpha} - \boldsymbol{\mu}_{\boldsymbol{\alpha}}), \tag{26}$$

$$\boldsymbol{\Sigma}_{\boldsymbol{\beta}c} = \boldsymbol{\Sigma}_{\boldsymbol{\beta}} - \boldsymbol{\Sigma}_{\boldsymbol{\beta\alpha}} \boldsymbol{\Sigma}_{\boldsymbol{\alpha}}^{-1} \boldsymbol{\Sigma}_{\boldsymbol{\alpha\beta}}, \tag{27}$$

where $\mu_{\boldsymbol{\beta}c}$ is a function of $\boldsymbol{\alpha}$ and $\Sigma_{\boldsymbol{\beta\alpha}}$ is constant. Therefore, for correlated normal variables, (23) becomes

$$\begin{aligned} S_{\boldsymbol{\alpha}} = & \frac{1}{D}\left[\int_{\mathbb{R}^s} \phi_s(\boldsymbol{\alpha})\, \mathrm{d}\boldsymbol{\alpha} \left[\int_{\mathbb{R}^{n-s}} f(\boldsymbol{\alpha}, \bar{\boldsymbol{\beta}}) \phi_{n-s}\left(\boldsymbol{\alpha}, \bar{\boldsymbol{\beta}} | \boldsymbol{\alpha}\right) \mathrm{d}\bar{\boldsymbol{\beta}} \right.\right. \\ & \left.\left. \times \int_{\mathbb{R}^{n-s}} f\left(\boldsymbol{\alpha}, \bar{\boldsymbol{\beta}}'\right) \phi_{n-s}\left(\boldsymbol{\alpha}, \bar{\boldsymbol{\beta}}' | \boldsymbol{\alpha}\right) \mathrm{d}\bar{\boldsymbol{\beta}}' \right] - f_0^2 \right], \end{aligned} \tag{28}$$

where ϕ_s and ϕ_{n-s} are the PDFs of the s- and $(n-s)$-dimensional multivariate normal variables, respectively.

C. GSA for Non-Gaussian Variables

The accuracy of the GSA depends on the accuracy of the correlation modeling. The Gaussian copula is the most widely used method employed for simulating non-Gaussian variables with correlations. Equation (28) is derived under the Gaussian assumption, the wind speeds and solar radiations, however, are non-Gaussian variables. Therefore, we apply the Gaussian copula to the GSA of the IES. For the non-Gaussian input variables, let us first define their associated Gaussian copula as [39]

$$\begin{aligned} C\left(u_1, u_2, \ldots, u_n; \boldsymbol{\rho}\right) = & \Phi_N\left(\Phi^{-1}\left(u_1\right), \Phi^{-1}\left(u_2\right), \ldots, \right. \\ & \left. \Phi^{-1}\left(u_n\right)\right), \end{aligned} \tag{29}$$

where $(u_1, u_2, \ldots, u_n)$ are the n-dimensional uniform distributions. Φ_N denotes the cumulative probability distribution function (CPDF) of n-dimensional multivariate standard normal variables with the correlation matrix $\boldsymbol{\rho}$. Φ^{-1} denotes the inverse CDF of the univariate standard normal distribution. By applying the cumulative probability distribution function, the input variable x_i following arbitrary distributions can be transformed into the standard Gaussian variable ξ_i through a uniform distribution, u_i, as

$$\xi_i = \Phi^{-1}\left(u_i\right) \;\; i = 1, \ldots, n, \tag{30}$$

The original input variables can be expressed via the inverse transformation as

$$R_i = F_i^{-1}(\xi_i) \;\; i = 1, \ldots, n, \tag{31}$$

where F_i denotes the CDF of the ith input variable. Applying (29), (30) and (31), S_y for correlated non-normal variables tends to be

$$\begin{aligned} S_y = & \frac{1}{D}\left[\int_{\mathbb{R}^s} \phi_s(\boldsymbol{\alpha})\, \mathrm{d}\boldsymbol{\alpha} \left[\int_{\mathbb{R}^{n-s}} f(\boldsymbol{y}, \bar{\boldsymbol{z}}) \phi_{n-s}\left(\boldsymbol{\alpha}, \bar{\boldsymbol{\beta}} | \boldsymbol{\alpha}\right) \mathrm{d}\bar{\boldsymbol{\beta}} \right.\right. \\ & \left.\left. \times \int_{\mathbb{R}^{n-s}} f\left(\boldsymbol{y}, \bar{\boldsymbol{z}}'\right) \phi_{n-s}\left(\boldsymbol{\alpha}, \bar{\boldsymbol{\beta}}' | \boldsymbol{\alpha}\right) \mathrm{d}\bar{\boldsymbol{\beta}}' \right] - f_0^2 \right], \end{aligned} \tag{32}$$

where

$$\begin{aligned} \boldsymbol{y} &= \left(F_1^{-1}\left(\Phi(\xi_1)\right), \ldots, F_s^{-1}\left(\Phi(\xi_s)\right)\right), \\ \bar{\boldsymbol{z}} &= \left(F_1^{-1}\left(\Phi(\bar{\xi}_1)\right), \ldots, F_{(n-s)}^{-1}\left(\Phi(\bar{\xi}_{(n-s)})\right)\right). \end{aligned} \tag{33}$$

Discussion. *Note that the Sobol index is generally applicable for any form of input random variables given the PDFs and correlations. Since the expression of S_y for the correlated variables is complicated, it typically requires a double-loop sampling strategy for the MCS. More specifically, the outer-loop samples are drawn from the target input variable, $\boldsymbol{y}$, while the inner-loop samples are drawn from the conditioned complementary variables, $\bar{\boldsymbol{z}}$. Clearly, this would require the traditional MCS to evaluate large amounts of samples, which can be computationally prohibitive, making GSA unsuitable for use in IES. For more details, the reader is referred to [11], [40].*

IV. A Novel GSA Computational Strategy Based on Generalized Unscented Transformation

The MCS suffers from a high computational burden to estimate the integration value in (32). This motivates us to design a cost-effective, double-loop GenUT-based approach [40].

A. The Proposed GenUT for UQ in the IES

1) Limitation of TUT

Although TUT can propagate uncertainties by approximating moments of input variables through a nonlinear function, it is developed under the Gaussian assumption and can only match the first two moments of input variables with an arbitrary distribution, and the weight associated with the sigma point is set artificially [41], [42]. Unlike the TUT, the GenUT can preserve more information through the diagonal components of the skewness and kurtosis, which better characterize higher-moment information with the same number of sigma points as the TUT method.

2) The Proposed GenUT

The crucial step of the GenUT method involves generating $2n+1$ critical samples, known as sigma points, to match the moments of n input variables. They can be obtained through

$$\begin{aligned} \boldsymbol{\chi}^0 &= \overline{\boldsymbol{x}}, & \boldsymbol{w}^0, \\ \boldsymbol{\chi}^i &= \overline{\boldsymbol{x}} - \boldsymbol{a}_i \sqrt{\boldsymbol{P}}_{[i]}, & \boldsymbol{w}', \\ \boldsymbol{\chi}^{i+n}, &= \overline{\boldsymbol{x}} + \boldsymbol{b}_i \sqrt{\boldsymbol{P}}_{[i]}, & \boldsymbol{w}'', \end{aligned} \tag{34}$$

for $i \in \{1, \ldots, n\}$. Here, $\boldsymbol{\chi}^{\boldsymbol{i}}$ is the ith sigma point. $\boldsymbol{a}$ and $\boldsymbol{b}$ are parameters that reflect the moments of the input variables. $\boldsymbol{w}$ are the weights associated with sigma points. $\overline{\boldsymbol{x}}$ is the

mean vector of the input variables. $\sqrt{\boldsymbol{P}}_{[i]}$is the ith column of $\sqrt{\boldsymbol{P}}$, which can be calculated by Cholesky decomposition. The moments of sigma points should be equal to those of the input variables. Thus, we have

$$\begin{aligned} E[\boldsymbol{\chi}] &= \overline{\boldsymbol{x}}, \\ E\left[(\boldsymbol{\chi}-\overline{\boldsymbol{x}})(\boldsymbol{\chi}-\overline{\boldsymbol{x}})^{\intercal}\right] &= \boldsymbol{P}, \\ E\left[(\boldsymbol{\chi}-\overline{\boldsymbol{x}})^{\odot 3}\right] &= \check{\boldsymbol{S}}, \\ E\left[(\boldsymbol{\chi}-\overline{\boldsymbol{x}})^{\odot 4}\right] &= \check{\boldsymbol{K}}. \end{aligned} \tag{35}$$

Here, $\odot$ represents the Hadamard product. $\check{\boldsymbol{S}}$ is the diagonal component of the skewness tensor denoted as $\check{\boldsymbol{S}} = [S_{111}, S_{222}, \ldots, S_{nnn}]^{\intercal}$, and $\check{\boldsymbol{K}}$ is the diagonal component of the kurtosis tensor denoted as $\check{\boldsymbol{K}} = [K_{1111}, K_{2222}, \ldots, K_{nnnn}]^{\intercal}$. By simplifying (35), we have constraint equations for parameters $\boldsymbol{a}$, $\boldsymbol{b}$ and weights $\boldsymbol{w}$ as

$$\begin{aligned} \sum_{i=0}^{2n} \boldsymbol{w}_i &= 1, \\ -\boldsymbol{w}' \odot \boldsymbol{a} + \boldsymbol{w}'' \odot \boldsymbol{b} &= \boldsymbol{0}, \\ \boldsymbol{w}' \odot \boldsymbol{a}^{\odot 2} + \boldsymbol{w}'' \odot \boldsymbol{b}^{\odot \boldsymbol{2}} &= \boldsymbol{1}, \\ -\boldsymbol{w}' \odot \boldsymbol{a}^{\odot 3} + \boldsymbol{w}'' \odot \boldsymbol{b}^{\odot 3} &= \sqrt{\boldsymbol{P}}^{\odot -3} \check{\boldsymbol{S}}. \end{aligned} \tag{36}$$

Then, we set $\boldsymbol{a}$ as the free parameters. After simplifying (36), we have

$$\boldsymbol{a}^{\odot 2} + \boldsymbol{S}\sqrt{\boldsymbol{P}}^{\odot -3}\boldsymbol{a} + \boldsymbol{S}^{\odot 2}\boldsymbol{P}^{\odot -3} - \boldsymbol{K}\boldsymbol{P}^{\odot -2} = \boldsymbol{0}. \tag{37}$$

Obviously, it is a quadratic form of $\boldsymbol{a}$ that yields

$$\boldsymbol{a} = \frac{1}{2}\left(-\sqrt{\boldsymbol{P}}^{\odot -3}\check{\boldsymbol{S}} + \sqrt{4\sqrt{\boldsymbol{P}}^{\odot -4}\check{\boldsymbol{K}} - 3\left(\sqrt{\boldsymbol{P}}^{\odot -3}\check{\boldsymbol{S}}\right)^{\odot 2}}\right). \tag{38}$$

Also, using (36), we have the relationships among free parameters $\boldsymbol{a}$ and $\boldsymbol{b}$ through

$$\boldsymbol{b} = \boldsymbol{a} + \sqrt{\boldsymbol{P}}^{\odot -3}\check{\boldsymbol{S}}. \tag{39}$$

Similarly, the relationships among $\boldsymbol{w}$, $\boldsymbol{a}$, and $\boldsymbol{b}$ hold for

$$\begin{aligned} \boldsymbol{w}'' &= \boldsymbol{1} \oslash \boldsymbol{b} \oslash (\boldsymbol{a}+\boldsymbol{b}), \\ \boldsymbol{w}' &= \boldsymbol{w}'' \odot \boldsymbol{b} \oslash \boldsymbol{a}, \end{aligned} \tag{40}$$

where $\oslash$ represents the Hadamard division. Up to this point, we can evaluate the PEF using the GenUT-based sigma points as

$$\boldsymbol{\mathcal{Y}}^i = \boldsymbol{f}\left(\boldsymbol{\chi}^i\right), \tag{41}$$

$$\overline{\boldsymbol{y}} = \sum_{i=0}^{2n} \boldsymbol{w}^i \boldsymbol{\mathcal{Y}}^i, \tag{42}$$

$$\boldsymbol{P}_y = \sum_{i=0}^{2n} \boldsymbol{w}^i \left(\boldsymbol{\mathcal{Y}}^i - \overline{\boldsymbol{y}}\right)\left(\boldsymbol{\mathcal{Y}}^i - \overline{\boldsymbol{y}}\right)^{\intercal}. \tag{43}$$

Since GenUT is applicable for correlated variables, we can sample from the uncertainties in the IES directly. Then, (41)-(43) are applied to approximate the total expectation, f_0, and total variance, D, for the operating states of the IES.

B. The Proposed Double-loop-based GSA using GenUT

To further utilize GenUT for GSA, we need to merge it into the double-loop sampling scheme.

1) Outer-loop Sampling

Now, based on (26), the mean of the conditioned variables, $\mu_{\boldsymbol{\beta}c}$, is a function of the conditioning variable, $\boldsymbol{\alpha}$. Thus, we can first sample from the conditioning variable, $\boldsymbol{\alpha}$, using (34) as the outer layer. Since $\boldsymbol{\alpha}$ only has one dimension for the first-order Sobol index, we get 3 sigma points as $\boldsymbol{\chi}_{\boldsymbol{\alpha}} = (\chi^0_{\boldsymbol{\alpha}}, \chi^1_{\boldsymbol{\alpha}}, \chi^2_{\boldsymbol{\alpha}})$ as well as the associated weights as $\boldsymbol{\omega}_{\boldsymbol{\alpha}} = (\omega^0_{\boldsymbol{\alpha}}, \omega^1_{\boldsymbol{\alpha}}, \omega^2_{\boldsymbol{\alpha}})$. Then, we can calculate the conditional expectation, $\mu_{\boldsymbol{\beta}c}$, for each value in $\boldsymbol{\chi}_{\boldsymbol{\alpha}}$ as

$$\begin{aligned} \boldsymbol{\mu}^0_{\boldsymbol{\beta}c} &= \boldsymbol{\mu}_{\boldsymbol{\beta}} + \boldsymbol{\Sigma}_{\boldsymbol{\beta}\boldsymbol{\alpha}}\boldsymbol{\Sigma}^{-1}_{\boldsymbol{\alpha}}(\chi^0_{\boldsymbol{\alpha}} - \mu_{\boldsymbol{\alpha}}), \\ \boldsymbol{\mu}^1_{\boldsymbol{\beta}c} &= \boldsymbol{\mu}_{\boldsymbol{\beta}} + \boldsymbol{\Sigma}_{\boldsymbol{\beta}\boldsymbol{\alpha}}\boldsymbol{\Sigma}^{-1}_{\boldsymbol{\alpha}}(\chi^1_{\boldsymbol{\alpha}} - \mu_{\boldsymbol{\alpha}}), \\ \boldsymbol{\mu}^2_{\boldsymbol{\beta}c} &= \boldsymbol{\mu}_{\boldsymbol{\beta}} + \boldsymbol{\Sigma}_{\boldsymbol{\beta}\boldsymbol{\alpha}}\boldsymbol{\Sigma}^{-1}_{\boldsymbol{\alpha}}(\chi^2_{\boldsymbol{\alpha}} - \mu_{\boldsymbol{\alpha}}). \end{aligned} \tag{44}$$

2) Inner-loop Sampling

Next, we sample the conditioned variables as the inner layer with the total dimension for the sigma points of $2(n-1)$. Here, note that two groups of samples, namely, $\bar{\boldsymbol{\beta}}$ and $\bar{\boldsymbol{\beta}}'$, are required as shown in (28). They have the same statistics and are independent of each other, which leads to

$$\boldsymbol{\mu}^k_{(\bar{\boldsymbol{\beta}},\bar{\boldsymbol{\beta}}')} = \begin{bmatrix} \boldsymbol{\mu}^k_{\boldsymbol{\beta}c} \\ \boldsymbol{\mu}^k_{\boldsymbol{\beta}c} \end{bmatrix}, \boldsymbol{\Sigma}_{(\bar{\boldsymbol{\beta}},\bar{\boldsymbol{\beta}}')} = \begin{bmatrix} \boldsymbol{\Sigma}_{\boldsymbol{\beta}c} & 0 \\ 0 & \boldsymbol{\Sigma}_{\boldsymbol{\beta}c} \end{bmatrix}, \tag{45}$$

for $k \in \{0,1,2\}$. Here, $\boldsymbol{\mu}^k_{(\bar{\boldsymbol{\beta}},\bar{\boldsymbol{\beta}}')}$ and $\boldsymbol{\Sigma}_{(\bar{\boldsymbol{\beta}},\bar{\boldsymbol{\beta}}')}$ are the expectation and covariance matrix of $(\bar{\boldsymbol{\beta}},\bar{\boldsymbol{\beta}}')$, respectively, under the condition of $\chi^k_{\boldsymbol{\alpha}}$. Then, we sample from $(\bar{\boldsymbol{\beta}},\bar{\boldsymbol{\beta}}')$ using GenUT as

$$\begin{aligned} \boldsymbol{\chi}^0_k &= \boldsymbol{\mu}^k_{(\bar{\boldsymbol{\beta}},\bar{\boldsymbol{\beta}}')}, & \boldsymbol{\omega}^0_{\bar{\boldsymbol{\beta}}(k)}, \\ \boldsymbol{\chi}^i_k &= \boldsymbol{\mu}^k_{(\bar{\boldsymbol{\beta}},\bar{\boldsymbol{\beta}}')} - \boldsymbol{a}_i\sqrt{\boldsymbol{\Sigma}_{(\bar{\boldsymbol{\beta}},\bar{\boldsymbol{\beta}}')}}_{[i]}, & \boldsymbol{\omega}^i_{\bar{\boldsymbol{\beta}}(k)}, \\ \boldsymbol{\chi}^{i+2(n-1)}_k &= \boldsymbol{\mu}^k_{(\bar{\boldsymbol{\beta}},\bar{\boldsymbol{\beta}}')} + \boldsymbol{b}_i\sqrt{\boldsymbol{\Sigma}_{(\bar{\boldsymbol{\beta}},\bar{\boldsymbol{\beta}}')}}_{[i]}, & \boldsymbol{\omega}^{i+2(n-1)}_{\bar{\boldsymbol{\beta}}(k)}, \end{aligned} \tag{46}$$

for $i \in \{1,\ldots,2(n-1)\}$ and $k \in \{0,1,2\}$. $\boldsymbol{a}_i$ and $\boldsymbol{b}_i$ can be obtained from (38) and (39). Then, the sigma points are divided into two groups, i.e., $(\boldsymbol{\chi}_{\bar{\boldsymbol{\beta}}(k)}, \boldsymbol{\chi}'_{\bar{\boldsymbol{\beta}}(k)})$, corresponding to $(\bar{\boldsymbol{\beta}},\bar{\boldsymbol{\beta}}')$.

3) Calculating the Sobol Index

Now, to evaluate the responses of the IES, we need to transform the Gaussian distributed $\boldsymbol{\alpha}$ and $\boldsymbol{\beta}$ into physical space. To do so, using (33), $\boldsymbol{\chi}_{\bar{\boldsymbol{\beta}}(k)}, \boldsymbol{\chi}_{\bar{\boldsymbol{\beta}}'(k)}$ and $\chi_{\boldsymbol{\alpha}}$ can be transformed into $\boldsymbol{\chi}_{\bar{\boldsymbol{z}}(k)}$, $\boldsymbol{\chi}_{\bar{\boldsymbol{z}}'(k)}$, and $\boldsymbol{\chi}_y$ that can be directly computed in the PEF model as

$$\begin{aligned} \boldsymbol{g}^j_k &= \boldsymbol{f}(\boldsymbol{\chi}^k_{\boldsymbol{y}}, \boldsymbol{\chi}^j_{\bar{\boldsymbol{z}}(k)}), \\ \boldsymbol{g}'^j_k &= \boldsymbol{f}(\boldsymbol{\chi}^k_{\boldsymbol{y}}, \boldsymbol{\chi}^j_{\bar{\boldsymbol{z}}'(k)}), \end{aligned} \tag{47}$$

for $j \in \{0,1,\ldots,4(n-1)\}$ and $k \in \{0,1,2\}$.

According to (32), S_y for correlated non-normal variables sampling by double-loop GenUT can be presented in the following form:

$$S_y = \frac{1}{D}\left[\sum_{k=0}^{2}\boldsymbol{\omega}^k_{\boldsymbol{\alpha}}\sum_{j=0}^{4(n-1)}\boldsymbol{\omega}^j_{\boldsymbol{\beta}(k)}\boldsymbol{g}^j_k\boldsymbol{g}'^j_k - f_0^2\right]. \tag{48}$$

4) Computational Burden Analysis

The computing time of this GSA is mainly determined by the total number of realizations, N_{GenUT}, of the energy flow model. Under our proposed GenUT-based double-loop scheme, to estimate S_y for n variables, N_{GenUT} is

$$N_{\text{GenUT}} = n \times 3 \times [2 \times 2(n-1)+1]. \tag{49}$$

More specifically, in the inner layer, there are two groups of conditioned variables $(\bar{z}, \bar{z}')$. Since both $\bar{z}$ and $\bar{z}'$ have $n-1$ dimensions, the dimension of the inner layer is $2(n-1)$, generating $2 \times 2 \times (n-1)+1$ sigma points. Also, the outer layer only has one variable that generates $2 \times 1 + 1 = 3$ sigma points. So, analyzing S_y for one variable requires evaluating the energy flow for $3 \times [2 \times 2 \times (n-1)+1]$ times. Therefore, to analyze S_y for all the n variables, N_{GenUT} is $n \times 3 \times [2 \times 2 \times (n-1)+1]$ as shown in (49).

Remark 2. *GenUT sampling is suitable for GSA. Although GenUT cannot provide the entire PDF of the output, the GSA only needs the expectation and variance of the outputs, which can be accurately approximated by GenUT. The proposed double-loop GenUT sampling strategy for GSA generates only a few samples compared to MCS. This enables us to evaluate the GSA for the IES cost-effectively while providing all the information required for calculating the Sobol index. The procedure of the proposed GenUT-based GSA is summarized in Fig. 3.*

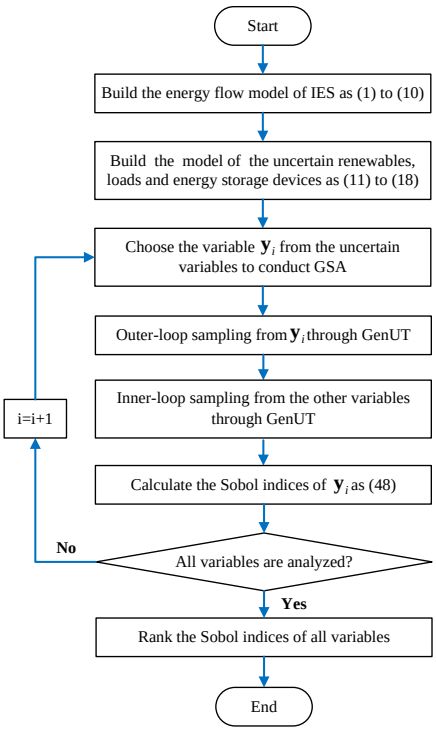

Fig. 3: Overall flowchart of proposed method.

V. Simulation Results

In this section, we test the performance of the proposed method using the two IESs based on the IEEE 30 and 118-bus systems, both of which consist of a power system and several district HNs.

A. Demo with the IES based on the IEEE 30-bus system

1) The Test System

First, a relatively small-scale IES is constructed to evaluate the performance of the proposed method. As shown in Fig. 4, IES consists of an IEEE 30-bus power system and 3 modified Barry Island 35-node district HNs as subsystems [43]. We select active power flows through Line 2-6 (i.e., P_{2-6}) as the output variable. The power system and 3 HNs are coupled through 2 backpressure CHPs at Buses 13, 22, and 1 regenerative electric boiler at Bus 7. The heat-to-power ratio of CHP is set to 1.3, and the efficiency of an electric boiler is set to 0.8 [43]. Assume that all heat loads in the same HN are aggregated as one uncertainty source. Therefore, they are modeled as three Gaussian variables in this case. Each district heating subsystem's total base heat load is 10.8 MW. Also, let us assume that all heat loads follow a normal distribution with a mean value equal to the base loads and a standard deviation equal to 20% of the mean values. Besides, we consider the uncertainty of 3 electrical loads located at Bus 2, Bus 7, and Bus 12, named EL 1, EL 2, and EL 3, respectively. Uncertain electrical loads are assumed to follow a normal distribution with a mean value equal to the base loads and a standard deviation equal to 10% of the mean values.

For every HN, Source 1 is selected as the slack node, which serves as the coupling node connected to the power system. Its slack node Bus 1 does not serve as the coupling node in the power system. Therefore, the electric boiler at Bus 7 is equivalent to the electric load of the power system, and the backpressure CHPs at Buses 13 and 22 are equivalent to the generators of the power system. The active power of the coupling nodes is determined by the heat loads of the HNs.

To assess the efficiency and accuracy of the GenUT-based GSA, the results of the proposed method are compared with the results of the MCS-based GSA with a sample size of 5,000.

2) GSA with Independent Loads

In this section, we evaluate the importance of independent heat loads and electrical loads for their impact on the power system. First, we compare the performance of the proposed GenUT-based GSA and the PCE-based GSA. Then, we conduct LSA and distinguish the differences between LSA and GSA.

a) Comparsion with the PCE

We use the MCS as the baseline method to compare the proposed GenUT method with the PCE method. The GSA results obtained by GenUT are 0.308, 0.126 0.169, 0.015, 0.286, and 0.073. The GSA results obtained by PCE are 0.309, 0.126, 0.169, 0.015, 0.303, and 0.078. The GSA results obtained by MCS are 0.320, 0.124, 0.167, 0.012, 0.279, and 0.076. Note that the Sobol index of the fourth variable has a tiny value, which indicates that the input variable has a negligible effect on the output variable. In this scenario, the error of the Sobol index of the fourth variable can be ignored. The mean error of the rest variables obtained by the GenUT is 2.6%. The mean error of the other variables obtained by the PCE is 3.5%. The simulation time for the GenUT and PCE methods are 2.02 s and 3.91 s, respectively.

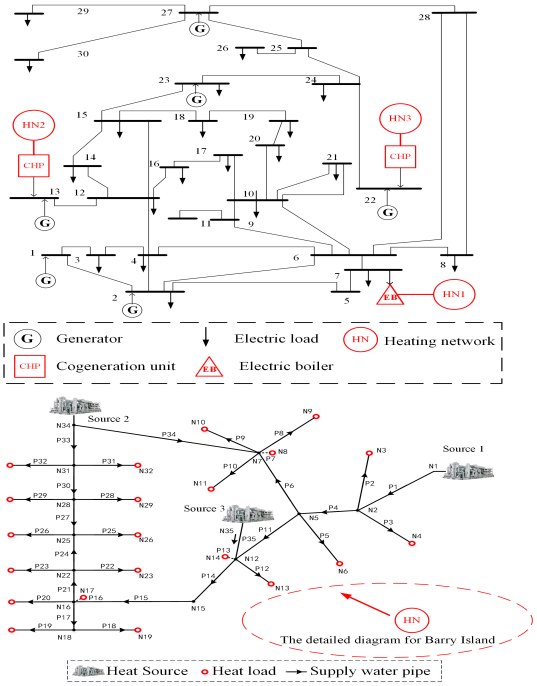

Fig. 4: Schematic diagram of IES based on the IEEE 30-bus system with 3 HNs (left) as well as the detailed diagram for Barry Island (right) of each HN.

The results show that the proposed GenUT-based GSA is more accurate and efficient than the PCE-based GSA. The reason lies in the fact that the PCE is a surrogate-based UQ method. So, it takes extra time to build the surrogate model. However, GenUT is based on moment information propagation through the physical model. This leads to an apparent decrease in computing costs. In addition, when the input probabilistic distribution changes, only the moment information needs to be modified. Therefore, GenUT-based GSA is easy to implement.

b) Comparison with the LSA

It should be emphasized that the LSA method is solely applicable to its specific operation point. The evaluation results vary significantly at different operation points. It is commonly acknowledged that this tool is ill-suited for a system where the operation points are randomly located.

Here, let us demonstrate this property for the LSA at two different operating points of the IES. In the first operating point, the loads are set to their base values. In the second operating point, the loads have a 20% perturbation relative to the base value. The LSA is calculated by the derivative of the system output corresponding to the inputs. The LSA index of the ith input variable is defined as $L_i = |\Delta g/\Delta x_i|$, where Δx_i stands for the small deviation of the ith uncertain load, Δg stands for the small deviation of the output caused by the small deviation of the inputs. The LSA indices of the first operating point are 0.055, 0.313, 0.240, 0.300, 0.224, and 0.263. The LSA indices of the second operating point are 0.053, 0.385, 0.235, 0.353, 0.215, and 0.251. These two operation points lead to totally different LSA results. This is the intrinsic limitation that LSA cannot address when facing uncertain inputs that might exhibit different operation points.

In essence, the LSA is based on the derivative of the system output only at the specific operation point, while the GSA is based on the variance quantification of the system output, which can naturally account for all possible operation points through its statistical inputs. These two kinds of sensitivity are fundamentally different. Therefore, the indices of the LSA and the GSA cannot be compared. In addition, the IES operating point varies when considering uncertain inputs. The simulation results show that the LSA indices change with different operating points. Therefore, GSA is more suitable for evaluating the IES system when considering uncertain inputs.

3) GSA with Different Correlations among Loads

To comprehensively analyze the impacts of correlated heat loads and electrical loads on power systems, the correlation coefficients of electrical loads are all set at 0.6. The correlation coefficients between heat loads in HNs 1 and 3 (i.e., ρ_{13}) and in HNs 2 and 3 (i.e., ρ_{23}) are both set at 0.4 while the correlation coefficient between heat loads in HNs 1 and 2 (i.e., ρ_{12}) increases from -0.6 to 0.6 with an interval of 0.2. The correlation matrix of heat loads in different HNs and electrical loads is shown by

$$\mathbf{r} = \begin{bmatrix} 1 & \rho_{12} & 0.4 & & & \\ \rho_{12} & 1 & 0.4 & & \mathbf{0} & \\ 0.4 & 0.4 & 1 & & & \\ & & & 1 & 0.6 & 0.6 \\ & \mathbf{0} & & 0.6 & 1 & 0.6 \\ & & & 0.6 & 0.6 & 1 \end{bmatrix}. \tag{50}$$

In this part, the MCS method with a sample size of 10,000 provides the benchmark of the GSA results. Furthermore, the Latin hypercube sampling (LHS) technique is employed, using a sample size of 1,000, to compare against the proposed GenUT-based GSA. Figures 5–7 compare the S_y calculated by GenUT, MCS, and LHS methods, respectively. S_y of HNs 1 and 2 decrease and S_y of HN 3 and EL 1 to EL 3 increases with increasing ρ_{12}. When the correlation coefficient is 0.6, S_y of HNs 1 and 2 is close to 0, indicating that HN 3 and EL 1 to EL 3 have a more critical impact on P_{2-6}. The results reveal that variations in the correlation coefficients lead to changes in the S_y of the HNs. The reason is that the correlation coefficients between the heat loads influence the statistical characteristics of the operating states of the IES. Therefore, considering the correlation between random input variables is crucial to the ranking for the importance of input uncertainties.

4) Computing Accuracy

Then, the computing accuracy of different correlation levels is evaluated. The results obtained with the MCS are used as a benchmark. Table I shows the errors of the GenUT method for the total expectation, E, the total standard deviation, σ, and the average errors of S_y for P_{2-6} when the correlation between the heat loads of HN 1 and 2 increases from -0.6 to 0.6. The results show that the double-loop GenUT accurately conducts GSA with different correlations of the input variables. The average errors of S_y are contained within the interval of 2.2% to 5.3%. Moreover, the estimation of E and σ has a high level of accuracy. The average error of E is 0.054% while the average error of σ is 0.9%. The estimation of E has a higher accuracy than that of σ because the expectation is first-order statistics, while the variance is second-order statistics. So, it is easier for GenUT to estimate lower-order statistics.

5) Computing Efficiency

Our proposed method significantly decreases the computing time compared with the MCS and the LHS. The computation time of the three methods for the GSA evaluation is shown in Table II. The reason is that GenUT selects a small number of critical samples instead of randomly selecting a large number of samples. Therefore, the proposed method significantly alleviates the computational burden while preserving excellent computing accuracy.

TABLE I: Total Expectation, Total Variance Errors, and Average Errors of S_y of P_{2-6} with Different Correlation Levels

Correlation ρ_{12}	E error [%]	σ error [%]	S_y error [%]
-0.6	0.101	0.56	3.18
-0.4	0.153	0.92	4.29
-0.2	0.005	0.23	2.20
0	0.007	0.81	5.28
0.2	0.07	1.40	3.78
0.4	0.014	2.14	4.82
0.6	0.028	0.26	4.32

TABLE II: The Computation Time of IES based on the IEEE 30-bus System

	Proposed method	MCS	LHS
Time [s]	2.02	931.9	87.7

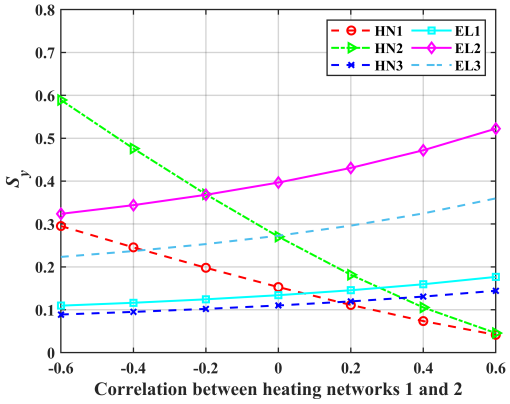

Fig. 5: S_y at different correlation ρ_{12} calculated by **GenUT**.

B. Application to the IEEE 118-bus-system-based IES

In this section, we evaluate the performance of the proposed method on the IES on a larger scale. The GenUT-based method is applied to IES based on the modified IEEE 118-bus system, which is shown in Fig. 8. IES consists of the IEEE 118-bus power system, 8 modified 35-node Barry Island district heating subsystems, 2 solar PVs, and 2 wind farms. Assume that the ambient temperature and the global heat transfer coefficient both follow a normal distribution with a mean equal to the base value and a standard deviation equal to 20% of the mean values. There are 14 sources of uncertainty in this case. The two solar PVs are named PV 1 and PV 2, and are connected to Bus 36 and Bus 54, respectively. The capacities of PV 1

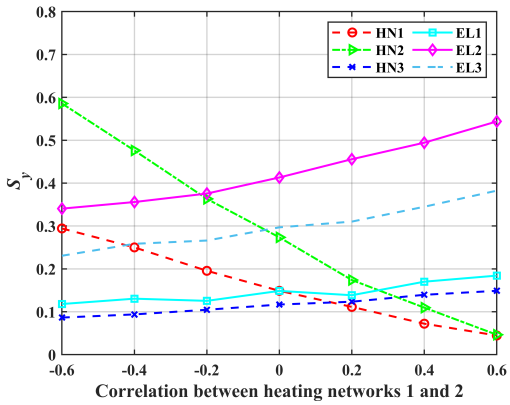

Fig. 6: S_y at different correlation ρ_{12} calculated by **MCS**.

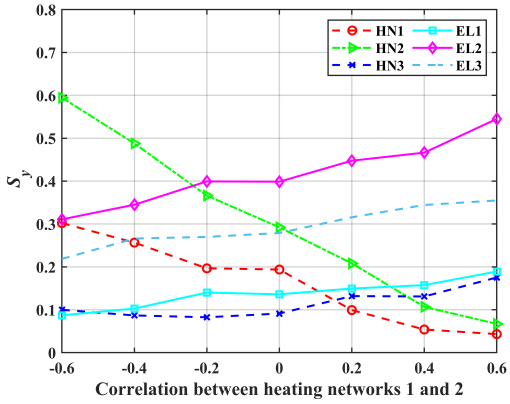

Fig. 7: S_y at different correlation ρ_{12} calculated by **LHS**.

and PV 2 are both 100 MW. The parameters κ are set to 0.9 and 0.8, respectively. The parameters ε are 0.9 and 0.8, respectively. The parameters of the solar PVs are cited from [28]. The two wind farms are named WF 1 and WF 2, and are connected to Bus 59 and Bus 88, respectively. The capacities of WF 1 and WF 2 are both 300 MW. The location parameters k are 1.5 and 1.7, respectively. The scale parameters λ are 8.1 and 8.5, respectively. The parameters of the wind farms are cited from [17]. Each renewable generation unit is connected to a battery for energy storage. The lower bound τ_{down} is 0.2, and the upper bound is 0.8. Assume that all batteries have adequate capacity. We neglect the dynamic process of charging and discharging the battery. The parameters of the batteries are cited from [35]. The power system and 8 HNs are coupled through 4 backpressure cogeneration units at Buses 10, 25, 49, and 65, 2 heat pumps at Buses 11 and 15, and 2 electric boilers at Buses 59 and 90. The heat-to-power ratio of CHP, an electric boiler's efficiency, and a heat pump's efficiency are set to 1.3, 0.8, and 3, respectively [44]. The correlation coefficients between the heat loads of each two HNs are set to 0.4. The correlation coefficient between WF 1 and WF 2 is set to 0.4. The correlation coefficient between PV 1 and PV 2 is set to 0.4.

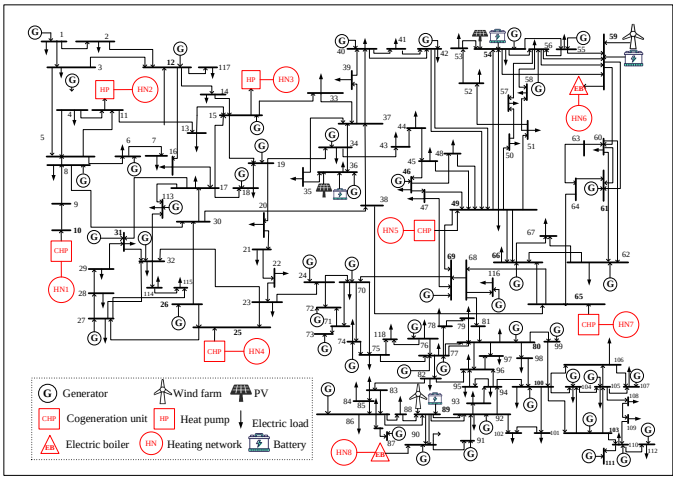

Fig. 8: Schematic diagram of the IES based on the IEEE 118-bus system.

1) GSA with Different Capacities of HNs

To comprehensively evaluate the impacts of heat loads on power systems, we consider 9 different levels of capacity of HNs. The total base heat loads of each HN are set to 10.8 MW, 21.6 MW, 43.2 MW, 64.8 MW, 108 MW, 216 MW, 324 MW, 432 MW, and 540 MW while keeping the correlation coefficients between variables unchanged. Assume that all heat loads follow a normal distribution with the mean value being the base value and the standard deviation equal to 20% of the mean values.

We select active power, P_{23-32}, as the output variable to analyze the S_y of WF 2, PV 2, HNs 1, HNs 3, the ambient temperature, and the global heat transfer coefficient. Figs. 9(a) and 9(c) show S_y calculated by the proposed GenUT method under different capacities. Fig. 9(a) regards batteries while Fig. 9(c) disregards batteries. When the capacities of the HNs are small, S_y of WF 2 is high, while S_y of the HNs 1 and 3 are close to 0. This makes sense since the loads in the HNs are quite small compared to the renewable generation capacity in this case. The uncertainty in wind farms and PVs is the main factor leading to the fluctuation of P_{23-32}. The S_y of HNs 1 and 3 increase as we increase the capacity of HNs, indicating that HNs have a greater impact on P_{23-32}. The S_y value of HN 1 stabilizes after the heat loads exceed 324 MW. This is because the S_y values of other HNs increase, thereby reducing the impact of HN 1. Comparing Figs. 9(a) and 9(c), the S_y of WF and PV both decrease when batteries are involved. These phenomena indicate that energy storage mitigates the uncertainties caused by renewable generation, reducing the importance of WFs and PVs.

2) GSA with Different Fluctuations of Uncertainties

We consider 9 degrees of fluctuation in HNs. Let us assume that all heat loads follow a normal distribution with mean values equal to the base loads of 324 MW, and the standard deviations, σ, equal to 1%, 3%, 5%, 7%, 10%, 15%, 20%, 25%, and 30% of the mean values while keeping the correlation coefficients among random variables unchanged.

We select active power, P_{23-32}, as the output variable to analyze S_y of WF 2, PV 2, HNs 1, HNs 3, the ambient temperature and the global heat transfer coefficient. Fig. 9(b) and 9(d) show S_y calculated by the proposed GenUT method under different fluctuations. Fig. 9(b) regards batteries, while Fig. 9(d) disregards batteries. When the fluctuation of HNs is small, S_y of WF 2 is high, while S_y of HNs 1 and 3 are close to 0. This means that the uncertainty of wind farms and PVs is the main factor that causes the fluctuation of P_{23-32}. The S_y of HNs 1 and 3 increase as we increase the capacity of HNs, indicating that HNs have a more critical impact on P_{23-32}. This indicates that S_y is related to the fluctuation levels of the input variables. If the fluctuation is greater, the input variable has a relatively greater impact on the output.

Simulation results also show that the Sobol index of ambient temperature and the global heat transfer coefficient are both nearly zero under different capacities and fluctuations of HNs. This means that the uncertainties of the two variables have little effect on the IES energy flow. This phenomenon arises from the small scale of the Barry Island district heating subsystems. The length of the pipe is relatively short, which leads to little heat loss. According to (1), the exponential term is still close to 1, even considering the uncertainties of ambient temperature and the global heat transfer coefficient.

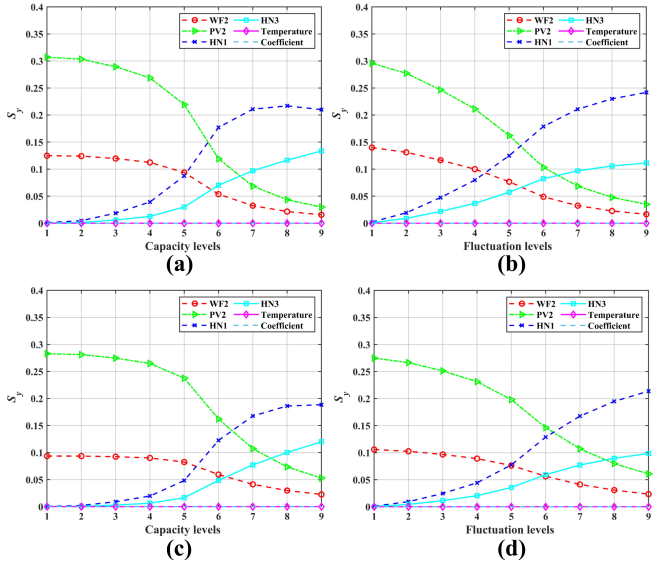

Fig. 9: Simulation results of the IES based on the IEEE 118-bus system under different cases. (a) S_y with respect to capacity levels of HNs with batteries included. (b) S_y with respect to fluctuation levels of HNs with batteries included. (c) S_y with respect to capacity levels of HNs with batteries excluded. (d) S_y with respect to fluctuation levels of HNs with batteries excluded.

3) Application of GenUT-based GSA for IES UQ

GSA can be utilized to implement dimensionality reduction when calculating the probabilistic energy flow of IES since it computes the importance ranking of uncertainties and identifies the sources of critical uncertainty. If we are interested in a specific output of the probabilistic energy flow (e.g., active power through a line), we can perform the GSA first; then, we only choose the critical inputs to calculate the probabilistic energy flow, which reduces the dimension of the uncertainties.

To demonstrate this, we set the mean value of the total heat load of each district heating subsystem as 324 MW with a standard deviation equal to 20% of the mean values. We choose active power flow, P_{23-32}, as output. The S_y values of all input variables calculated by the GenUT-based GSA are presented in Fig. 10.

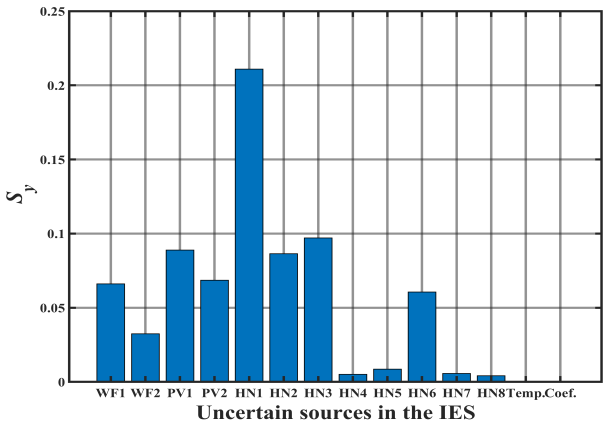

Fig. 10: S_y of all input variables.

There are 7 variables that have S_y larger than 0.05, they are WF 1, PV 1, PV 2, HN 1, HN 2, HN 3, and HN 6. The respective Sobol indices are 0.07, 0.09, 0.07, 0.21, 0.09, 0.1, and 0.06. We keep the uncertainty of the critical input variables unchanged while setting the other input variables as deterministic values equal to their own mean values. To assess the performance of the application, we established a benchmark considering all input variables. We calculated the relative errors of the mean and standard deviation when only the most significant uncertainty sources were taken into account, as presented in Table III. Note that GenUT with dimensionality reduction is abbreviated as GenUT-DR in Table III. It shows that when we reserve the first 7 critical variables, the standard deviation error is close to 9%. and the expectation error is almost zero. The 95% confidence level of P_{23-32} gained by MCS, GenUT, and GenUT with dimensionality reduction methods are $[76.3, 98.6]$, $[77.5, 97.1]$ and $[77.5, 97.0]$, respectively. In general, the results obtained by different methods are similar. However, note that the confidence intervals are calculated by the expectation and the variance of P_{23-32} under the Gaussian assumption. We can see small differences in the results due to the tiny error of the PEF result gained by GenUT and GenUT with dimensionality reduction compared with MCS. This result shows that the GSA can identify weak uncertainty sources that have little impact on the output. Their uncertainty can be ignored in PEF studies, reducing the dimension of the system.

TABLE III: Statistics for Different Number of Variables

Method	E	E error [%]	σ	σ error [%]
MCS	87.30	—	5.10	—
GenUT	87.28	0.030	4.99	1.94
GenUT-DR	87.26	0.046	4.96	2.65

VI. Further Discussions

A. Discussions on Confidence Intervals

For UQ, the GenUT provides the confidence intervals of the output probability distributions only under the Gaussian assumption. However, the GSA aims to rank the importance priority of the input variables related to the uncertainty of the model output, so confidence intervals are unnecessary in the GSA [10], [11].

B. Difference between PEF and Optimal Energy Flow (OEF)

The PEF aims to assess the statistical characteristics of the IES operating states under the uncertainties of loads and generations. However, the OEF focuses on the optimal operating state by optimizing the objective functions while satisfying the constraint equations [28], [45], [46]. The GSA is based on the uncertainty propagation technique that quantifies the variances generated in the output variables as a result of variations in the input variables. Therefore, PEF is applied in GSA rather than OEF.

C. Difference between GSA and the Feature Importance

It is necessary to distinguish between GSA and a similar concept, the feature importance. Machine learning-based feature importance is intended to score input features based on their usefulness in predicting a target variable [47]. The GSA apportions uncertainties of different loads and generations to uncertainties of the output IES operating states based on UQ. Consequently, the feature importance is fundamentally different from the GSA.

VII. Conclusions

In this paper, we propose a GenUT-based double-loop strategy that, for the first time, explores the GSA in the IES. First, the Gaussian copula is employed to model correlations among Gaussian and non-Gaussian variables. Second, the GenUT method accurately approximates the expectation and variance of the outputs by preserving higher-moment information of the inputs. Then, inner- and outer-loop sampling strategies are proposed to allow GenUT accessible in GSA with correlated input variables. The following conclusions can be drawn:

1) For the IES, the uncertainty of heating loads and renewable generation crucially alters the power system operation states. Moreover, the degree of effect relies on parameters of probability distributions and correlations among the input variables.
2) The proposed GenUT-based GSA achieves a speedup of two orders of magnitude compared with the MCS. Simulations in multiple IESs demonstrate its excellent performances in GSA.
3) The paper presents comparative experiments to identify the key factors that determine the Sobol index. The GSA is carried out with different statistical features of the uncertain input variables. Besides, it reveals the impact of energy storage on GSA in the IES.
4) The GSA identifies weak uncertain inputs, whose uncertainty has negligible impacts on output. This can be further utilized for the reduction of system dimensionality, which contributes to a more effective computation in PEF.

In the future, we plan to explore more scenarios in which the statistical features of heat demands and renewable generation rapidly change.

REFERENCES

[1] R. Yu, W. Gu, H. Lu, S. Yao, S. Zhang, S. Lu, S. Ding, and E. Luo, "Non-iterative calculation of quasi-dynamic energy flow in the heat and electricity integrated energy systems," *IEEE Trans. Power Syst.*, vol. 38, no. 5, pp. 4148–4164, Sep. 2023.

[2] L.-N. Liu and G.-H. Yang, "Distributed optimal energy management for integrated energy systems," *IEEE Trans. Ind. Informat.*, vol. 18, no. 10, pp. 6569–6580, Oct. 2022.

[3] X. Qin, H. Sun, X. Shen, Y. Guo, Q. Guo, and T. Xia, "A generalized quasi-dynamic model for electric-heat coupling integrated energy system with distributed energy resources," *Appl. Energy*, vol. 251, p. 113270, Oct. 2019.

[4] Q. Sun, Y. Fu, H. Lin, and R. Wennersten, "A novel integrated stochastic programming-information gap decision theory (IGDT) approach for optimization of integrated energy systems (IESs) with multiple uncertainties," *Appl. Energy*, vol. 314, p. 119002, May 2022.

[5] Y. Jiang, Z. Ren, Z. Sun, W. Li, and X. Yang, "A stochastic response surface method based probabilistic energy flow analysis method for integrated electricity and gas systems," *IEEE Trans. Power Syst.*, vol. 37, no. 3, pp. 2467–2470, May 2022.

[6] H. Liu, X. Shen, Q. Guo, H. Sun, M. Shahidehpour, W. Zhao, and X. Zhao, "Application of modified progressive hedging for stochastic unit commitment in electricity-gas coupled systems," *CSEE J. Power Energy Syst.*, vol. 7, no. 4, pp. 840–849, Jul. 2021.

[7] R. Preece and J. V. Milanović, "Assessing the applicability of uncertainty importance measures for power system studies," *IEEE Trans. Power Syst.*, vol. 31, no. 3, pp. 2076–2084, May 2016.

[8] C. Qin, Y. Jin, M. Tian, P. Ju, and S. Zhou, "Comparative study of global sensitivity analysis and local sensitivity analysis in power system parameter identification," *Energies*, vol. 16, no. 16, p. 5915, Aug. 2023.

[9] B. Qi, K. N. Hasan, and J. V. Milanović, "Identification of critical parameters affecting voltage and angular stability considering load-renewable generation correlations," *IEEE Trans. Power Syst.*, vol. 34, no. 4, pp. 2859–2869, Jul. 2019.

[10] S. Peng, X. Lin, J. Tang, K. Xie, F. Ponci, and A. Monti, "A set of novel global sensitivity analysis indices for probabilistic static voltage stability assessment with correlated uncertainty sources," *IEEE Trans. Power Syst.*, vol. 39, no. 2, pp. 2543–2557, Mar. 2024.

[11] X. Xu, Z. Yan, M. Shahidehpour, H. Wang, and S. Chen, "Power system voltage stability evaluation considering renewable energy with correlated variabilities," *IEEE Trans. Power Syst.*, vol. 33, no. 3, pp. 3236–3245, May 2018.

[12] H. Wang, Z. Yan, M. Shahidehpour, X. Xu, and Q. Zhou, "Quantitative evaluations of uncertainties in multivariate operations of microgrids," *IEEE Trans. Smart Grid*, vol. 11, no. 4, pp. 2892–2903, Jul. 2020.

[13] Z. Hu, Y. Xu, M. Korkali, X. Chen, L. Mili, and J. Valinejad, "A Bayesian approach for estimating uncertainty in stochastic economic dispatch considering wind power penetration," *IEEE Trans. Sustainable Energy*, vol. 12, no. 1, pp. 671–681, Jan. 2021.

[14] Y. Xu, Z. Hu, L. Mili, M. Korkali, and X. Chen, "Probabilistic power flow based on a Gaussian process emulator," *IEEE Trans. Power Syst.*, vol. 35, no. 4, pp. 3278–3281, Jul. 2020.

[15] K. Ye, J. Zhao, C. Huang, N. Duan, Y. Zhang, and T. E. Field, "A data-driven global sensitivity analysis framework for three-phase distribution system with PVs," *IEEE Trans. Power Syst.*, vol. 36, no. 5, pp. 4809–4819, Sep. 2021.

[16] M. Aien, M. Fotuhi-Firuzabad, and F. Aminifar, "Probabilistic load flow in correlated uncertain environment using unscented transformation," *IEEE Trans. Power Syst.*, vol. 27, no. 4, pp. 2233–2241, Nov. 2012.

[17] S. Peng, J. Tang, and W. Li, "Probabilistic power flow for AC/VSC-MTDC hybrid grids considering rank correlation among diverse uncertainty sources," *IEEE Trans. Power Syst.*, vol. 32, no. 5, pp. 4035–4044, Sep. 2017.

[18] S. Peng, X. Lin, J. Tang, K. Xie, F. Ponci, A. Monti, and W. Li, "Probabilistic power flow of AC/DC hybrid grids with addressing boundary issue of correlated uncertainty sources," *IEEE Trans. Sustainable Energy*, vol. 13, no. 3, pp. 1607–1619, Jul. 2022.

[19] S. J. Julier and J. K. Uhlmann, "A general method for approximating nonlinear transformations of probability distributions," Robotics Research Group, University of Oxford, Tech. Rep., 1996.

[20] D. Ebeigbe, T. Berry, M. M. Norton, A. J. Whalen, D. Simon, T. Sauer, and S. J. Schiff, "A generalized unscented transformation for probability distributions," 2021, arXiv:2104.01958.

[21] S. Kucherenko, S. Tarantola, and P. Annoni, "Estimation of global sensitivity indices for models with dependent variables," *Comput. Phys. Commun.*, vol. 183, no. 4, pp. 937–946, Apr. 2012.

[22] S. Zhang, W. Gu, H. Qiu, S. Yao, G. Pan, and X. Chen, "State estimation models of district heating networks for integrated energy system considering incomplete measurements," *Appl. Energy*, vol. 282, p. 116105, Jan. 2021.

[23] S. Yao, W. Gu, S. Lu, S. Zhou, Z. Wu, G. Pan, and D. He, "Dynamic optimal energy flow in the heat and electricity integrated energy system," *IEEE Trans. Sustainable Energy*, vol. 12, no. 1, pp. 179–190, Jan. 2021.

[24] G. P. Henze and A. G. Floss, "Evaluation of temperature degradation in hydraulic flow networks," *Energy Build.*, vol. 43, no. 8, pp. 1820–1828, Aug. 2011.

[25] M. Mohammadi, H. Basirat, and A. Kargarian, "Nonparametric probabilistic load flow with saddle point approximation," *IEEE Trans. Smart Grid*, vol. 9, no. 5, pp. 4796–4804, Sep. 2018.

[26] S. Zhang, W. Gu, S. Lu, S. Yao, S. Zhou, and X. Chen, "Dynamic security control in heat and electricity integrated energy system with an equivalent heating network model," *IEEE Trans. Smart Grid*, vol. 12, no. 6, pp. 4788–4798, Nov. 2021.

[27] S. Yao, W. Gu, J. Wu, H. Lu, S. Zhang, Y. Zhou, and S. Lu, "Dynamic energy flow analysis of the heat-electricity integrated energy systems with a novel decomposition-iteration algorithm," *Appl. Energy*, vol. 322, p. 119492, Sep. 2022.

[28] H. Sheng and X. Wang, "Probabilistic power flow calculation using non-intrusive low-rank approximation method," *IEEE Trans. Power Syst.*, vol. 34, no. 4, pp. 3014–3025, Jul. 2019.

[29] A. Shabanpour-Haghighi and M. Karimaghaei, "A Copula-Hammersley approach for probabilistic analysis of integrated power and heat networks," *Cleaner Energy Syst.*, vol. 4, p. 100051, Apr. 2023.

[30] H. Tian, H. Zhao, H. Li, C. Liu, J. Chen, and H. Zhang, "Interval-probabilistic electricity-heat-gas flow calculation by dual-level surrogate structure," *IEEE Trans. Smart Grid*, vol. 14, no. 6, pp. 4333–4344, Nov. 2023.

[31] C. Lin, Z. Bie, C. Pan, and S. Liu, "Fast cumulant method for probabilistic power flow considering the nonlinear relationship of wind power generation," *IEEE Trans. Power Syst.*, vol. 35, no. 4, pp. 2537–2548, Jul. 2020.

[32] Z. Xie, T. Ji, M. Li, and Q. Wu, "Quasi-Monte Carlo based probabilistic optimal power flow considering the correlation of wind speeds using copula function," *IEEE Trans. Power Syst.*, vol. 33, no. 2, pp. 2239–2247, Mar. 2018.

[33] M. Aien, M. Fotuhi-Firuzabad, and M. Rashidinejad, "Probabilistic optimal power flow in correlated hybrid wind–photovoltaic power systems," *IEEE Trans. Smart Grid*, vol. 5, no. 1, pp. 130–138, Jan. 2014.

[34] Y. Yang, S. Bremner, C. Menictas, and M. Kay, "Modelling and optimal energy management for battery energy storage systems in renewable energy systems: A review," *Renewable Sustainable Energy Rev.*, vol. 167, p. 112671, Oct. 2022.

[35] H. Chen, J. Shao, T. Jiang, X. Li, and R. Zhang, "Performance assessment of multiple-types co-located storage for uncertainty mitigation in integrated electric-gas system using generalized polynomial chaos," *Appl. Energy*, vol. 374, p. 123930, 2024.

[36] S. Zhang, S. Wang, Z. Zhang, J. Lyu, H. Cheng, M. Huang, and Q. Zhang, "Probabilistic multi-energy flow calculation of electricity–gas integrated energy systems with hydrogen injection," *IEEE Trans. Ind. Appl.*, vol. 58, no. 2, pp. 2740–2750, Mar.-Apr. 2021.

[37] A. Saltelli, "Making best use of model evaluations to compute sensitivity indices," *Comput. Phys. Commun.*, vol. 145, no. 2, pp. 280–297, May 2002.

[38] A. Saltelli, M. Ratto, T. Andres, F. Campolongo, J. Cariboni, D. Gatelli, M. Saisana, and S. Tarantola, *Global Sensitivity Analysis: The Primer*. John Wiley & Sons, 2008.

[39] G. Papaefthymiou and D. Kurowicka, "Using copulas for modeling stochastic dependence in power system uncertainty analysis," *IEEE Trans. Power Syst.*, vol. 24, no. 1, pp. 40–49, Feb. 2009.

[40] S. Xiao, Z. Lu, and F. Qin, "Estimation of the generalized Sobol's sensitivity index for multivariate output model using unscented transformation," *J. Struct. Eng.*, vol. 143, no. 5, p. 06016005, May 2017.

[41] H. M. Menegaz, J. Y. Ishihara, G. A. Borges, and A. N. Vargas, "A systematization of the unscented Kalman filter theory," *IEEE Trans. Autom. Control*, vol. 60, no. 10, pp. 2583–2598, Oct. 2015.

[42] L. Chang, B. Hu, A. Li, and F. Qin, "Unscented type Kalman filter:

Limitation and combination," *IET Signal Process.*, vol. 7, no. 3, pp. 167–176, May 2013.
[43] X. Liu, J. Wu, N. Jenkins, and A. Bagdanavicius, "Combined analysis of electricity and heat networks," *Appl. Energy*, vol. 162, pp. 1238–1250, Jan. 2016.
[44] S. Yao, W. Gu, J. Wu, M. Qadrdan, H. Lu, S. Lu, and Y. Zhou, "Fast and generic energy flow analysis of the integrated electric power and heating networks," *IEEE Trans. Smart Grid*, vol. 15, no. 1, pp. 355–367, Jan. 2024.
[45] J. Chen, H. Chen, Z. Liang, X. Zheng, D. Xiao, Y. Li, and H. Yan, "An exergy analysis model for the optimal operation of integrated heat-and-electricity-based energy systems," *Prot. Control Mod. Power Syst.*, vol. 9, no. 1, pp. 1–18, 2024.
[46] C. Zhang, Y. Xu, Z. Li, and Z. Y. Dong, "Robustly coordinated operation of a multi-energy microgrid with flexible electric and thermal loads," *IEEE Trans. Smart Grid*, vol. 10, no. 3, pp. 2765–2775, May 2019.
[47] A. Zien, N. Krämer, S. Sonnenburg, and G. Rätsch, "The feature importance ranking measure," in *Proc. Eur. Conf. Mach. Learn. Knowl. Discovery Databases*. Bled, Slovenia: Springer, Sept. 7-11, 2009, pp. 694–709.

Yibo Li (S'23) received the B.S. degree in electrical engineering from the College of Electrical and Information Engineering, Hunan University, Changsha, China, in 2023. He is currently working toward the Ph.D. degree in the School of Electrical Engineering from Southeast University, Nanjing, China. His research interests include integrated energy systems uncertainty quantification, and risk analysis.

Yijun Xu (SM'21) is a professor at Southeast University, Nanjing, China. He received his Ph.D. degree from the Bradley Department of Electrical and Computer Engineering at Virginia Tech, Falls Church, VA, in December 2018. He worked as a research assistant professor at Virginia Tech-Northern Virginia Center, Falls Church, VA, in 2021. He was a postdoc associate at the same institute from 2019 to 2020. He did a computation internship at Lawrence Livermore National Laboratory, Livermore, CA, and a power engineer internship at ETAP – Operation Technology, Inc., Irvine, California, in 2018 and 2015, respectively.

His research interests include power system uncertainty quantification, uncertainty inversion, and decision-making under uncertainty. Dr. Xu is currently serving as an Associate Editor of the IET GENERATION, TRANSMISSION & DISTRIBUTION, an Associate Editor of the IET RENEWABLE POWER GENERATION, and the Young Editor of the POWER SYSTEM PROTECTION AND CONTROL. He is the co-chair of the IEEE Task Force on Power System Uncertainty Quantification and Uncertainty-Aware Decision-Making.

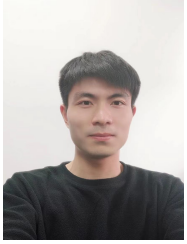

Shuai Yao (S'15-M'22) received his B.Eng. degree in Electrical Engineering from the Honors College, Nanjing Normal University, China, in 2017. In 2022, he received his Ph.D. degree from the School of Electrical Engineering, Southeast University, China. He is currently working as a Postdoctoral Research Associate with Cardiff University, Cardiff, UK. His research interests include modelling and simulation of power and energy systems, heat decarbonisation, and hydrogen integration for accelerated net zero transitions.

Wei Gu (M'06-SM'16) received his B.S. and Ph.D. degrees in Electrical Engineering from Southeast University, China, in 2001 and 2006, respectively. From 2009 to 2010, he was a Visiting Scholar in the Department of Electrical Engineering, Arizona State University.

He is now a professor at the School of Electrical Engineering, Southeast University. He is the director of the institute of distributed generations and active distribution networks. His research interests include distributed generations and microgrids, integrated energy systems. He is an Editor for the IEEE Transactions on Power Systems, the IET Energy Systems Integration and the Automation of Electric Power Systems (China).

Lamine Mili (LF'17) received the Ph.D. degree from the University of Liège, Belgium, in 1987. He is a Professor of Electrical and Computer Engineering, Virginia Tech, Blacksburg. He has five years of industrial experience with the Tunisian electric utility, STEG. At STEG, he worked in the planning department from 1976 to 1979 and then at the Test and Meter Laboratory from 1979 till 1981. He was a Visiting Professor with the Swiss Federal Institute of Technology in Lausanne, the Grenoble Institute of Technology, the École Supérieure D'électricité in France and the École Polytechnique de Tunisie in Tunisia, and did consulting work for the French Power Transmission company, RTE.

His research has focused on power system planning, risk management of complex systems to catastrophic failures, robust estimation and control, nonlinear dynamics, and bifurcation theory. He is the co-founder and co-editor of the *International Journal of Critical Infrastructure*. He is the chairman of the IEEE Working Group on State Estimation Algorithms and the chair of the IEEE Task Force on Power System Uncertainty Quantification and Uncertainty-Aware Decision-Making. He is a recipient of several awards including the US National Science Foundation (NSF) Research Initiation Award and the NSF Young Investigation Award.

Mert Korkali (SM'18) received a Ph.D. degree in electrical engineering from Northeastern University, Boston, MA, USA, in 2013. He has been an Assistant Professor in the Department of Electrical Engineering and Computer Science at the University of Missouri (MU) since 2022. Before joining MU, he worked as a Research Staff Member at Lawrence Livermore National Laboratory, Livermore, CA, USA, where he served as a principal investigator (PI) and co-PI on several projects on power grid operations and planning, solar-grid integration, and extreme event modeling, funded by the U.S. Department of Energy. Prior to that, he was a Postdoctoral Research Associate at the University of Vermont, Burlington, VT, USA.

His current research interests lie in the broad interface of power system state estimation, electromagnetic transient analysis, cascading failures, uncertainty quantification, and data-driven methods for power system operation, control, and planning. He received the Best Paper Award at the 2019 IEEE Power and Energy Society General Meeting (PESGM). He is the Chair of the IEEE PES Task Force (TF) on Standard Test Cases for Power System State Estimation and the Secretary of the IEEE PES TF on Power System Uncertainty Quantification and Uncertainty-Aware Decision-Making. Dr. Korkali is currently the Associate Editor of the IEEE TRANSACTIONS ON POWER SYSTEMS, IEEE OPEN ACCESS JOURNAL OF POWER AND ENERGY, IEEE POWER ENGINEERING LETTERS, *Journal of Modern Power Systems and Clean Energy*, and *ACM Transactions on Probabilistic Machine Learning*.

Shuai Lu (S'17-M'21) is currently a lecturer at the School of Electrical Engineering, Southeast University, Nanjing China. He received his B.S. degree in Smart Grid Information Engineering from Nanjing University of Science and Technology, Nanjing, China in 2016 and his Ph.D. degree in Electrical Engineering from Southeast University, Nanjing China, in 2021. From 2018 to 2019, he was a visiting scholar at the University of New South Wales, Sydney, Australia.

He is a Young Editorial Board Member of *Applied Energy* and *Electric Power Automation Equipment*. His research interests include integrated energy systems, operations research, and data-driven techniques in power systems.